



Progressive expansion of seafloor anoxia in the Middle to Late Ordovician Yangtze Sea: Implications for concurrent decline of invertebrate diversity



Junpeng Zhang ^{a,b,*}, Chao Li ^{a,c}, Xiang Fang ^a, Wenjie Li ^a, Yiyang Deng ^{a,c}, Chenyi Tu ^b, Thomas J. Algeo ^{d,e,f}, Timothy W. Lyons ^b, Yuandong Zhang ^{a,c}

^a State Key Laboratory of Palaeobiology and Stratigraphy, Nanjing Institute of Geology and Palaeontology and Center for Excellence in Life and Paleoenvironment, Chinese Academy of Sciences, Nanjing, Jiangsu 210008, China

^b Department of Earth and Planetary Sciences and Alternative Earths Astrobiology Center, University of California, Riverside, CA 92521, USA

^c University of Chinese Academy of Sciences, Beijing 100049, China

^d State Key Laboratory of Geological Processes and Mineral Resources, China University of Geosciences, Wuhan, Hubei 430074, China

^e State Key Laboratory of Biogeology and Environmental Geology, China University of Geosciences, Wuhan, Hubei 430074, China

^f Department of Geology, University of Cincinnati, Cincinnati, OH 45221-0013, USA

ARTICLE INFO

Article history:

Received 23 April 2022

Received in revised form 25 July 2022

Accepted 30 September 2022

Available online 12 October 2022

Editor: B. Wing

Keywords:
nitrogen isotopes
Mo isotopes
ocean redox
climatic cooling
GOBE
biodiversity

ABSTRACT

The Great Ordovician Biodiversification Event (GOBE) achieved its peak during the Middle Ordovician, likely in association with climatic cooling and a rise of atmospheric O₂. However, unstable redox states developed widely in contemporaneous epeiric seas, challenging previous assumptions about sustained oceanic oxygenation driven by deep-ocean ventilation in the aftermath of Ordovician cooling. Here, we investigate two Middle-Upper Ordovician shale-dominated successions from intra-shelf basin and slope settings of the Yangtze Sea, South China. Negative shifts in bulk δ¹⁵N and productivity proxies reveal temporal changes in the pattern of nutrient cycling under moderate-to-high productivity conditions, which were likely sustained by increased upwelling of cold and nutrient-rich deep waters in sync with contemporaneous climatic cooling. As a result, marine anoxia likely expanded in deep waters of the Yangtze Sea, as reflected in enrichments of highly reactive iron and redox-sensitive metals (Mo, U). Although moderate Mo abundances (25–50 ppm) and δ^{98/95}Mo values (+0.4 to +0.8‰) within the euxinic interval suggest that bottom waters had low sulfide concentrations, the δ^{98/95}Mo values are comparable with those of coeval euxinic facies (~+0.6‰). Furthermore, our modeling results show that low δ^{98/95}Mo can be produced when sulfidic sinks dominate Mo removal, suggesting that Middle-Late Ordovician oceans may have been less oxygenated than previously assumed, at least for the continental seas of South China, Baltica and Laurentia. These environmental changes may provide a new explanation for the ~50% decline of invertebrate species following the peak of GOBE. Our findings thus link the progressive expansion of marine anoxia and climatic cooling to a profound biotic change during the Mid-Late Ordovician Period.

© 2022 Elsevier B.V. All rights reserved.

1. Introduction

The Early and Middle Ordovician witnessed a series of important changes in the Earth system, including rising atmospheric O₂ and falling CO₂ levels, intense tectonic activity and related enhanced weathering, and subsequent long-term cooling—as well as

the Great Ordovician Biodiversification Event (GOBE) among marine invertebrates and the colonization of exposed continental surfaces by early land plants (Trotter et al., 2008; Young et al., 2009; Lenton et al., 2016; Edwards et al., 2017). In addition to increases in biodiversity, complex ecological structures and interactions were established during the GOBE, leading to increased stability of marine ecosystems (Servais et al., 2010). Several hypotheses have been proposed for the triggers of GOBE, such as secular cooling (Trotter et al., 2008) and increasing atmospheric oxygenation (Edwards et al., 2017), which are still under debate. Following the peak of GOBE, an abrupt decline in biodiversity of invertebrates occurred during the ~15 Myr interval of the Darriwilian to Sand-

* Corresponding author at: State Key Laboratory of Palaeobiology and Stratigraphy, Nanjing Institute of Geology and Palaeontology and Center for Excellence in Life and Paleoenvironment, Chinese Academy of Sciences, Nanjing, Jiangsu 210008, China.

E-mail address: jpzhang@nigpas.ac.cn (J. Zhang).

bian stages (Servais and Harper, 2018; Fan et al., 2020), although its causal connection to contemporaneous environmental changes remains unclear.

The middle Darriwilian carbon isotope excursion (MDICE) has been identified on several continents and interpreted as a perturbation of the global carbon cycle (Saltzman and Edwards, 2017). Contemporaneous decoupling of the oceanic carbon and sulfur cycles has been attributed to reorganization of the sulfur cycle driven by deep-ocean ventilation in response to long-term global cooling during the Ordovician (Kah et al., 2016; Young et al., 2016). Concurrently, colonization of early land plants likely enhanced nutrient delivery to the ocean and stimulated marine primary productivity (Lenton et al., 2016). Thus, the global ocean may not have been fully and stably oxygenated during the Ordovician, and recent studies have revealed spatial heterogeneity in ocean-redox conditions during the late Darriwilian to Sandbian (Kozik et al., 2019; Fang et al., 2020). At the same time, minor $\Delta^{33}\text{S}$ anomalies also suggest that anoxic deep waters may have impinged on shallow shelves and even impacted the habitability of continental ecosystems (Chen et al., 2020). However, beyond this limited evidence for shelf redox instability, it is not well known whether the open ocean experienced extensive oxygenation in phase with rising atmospheric O₂ levels (Edwards et al., 2017) due to a scarcity of geochemical proxy data that can track the secular evolution of global-ocean redox conditions, such as the $\delta^{98/95}\text{Mo}$ of euxinic shales (Dahl et al., 2010; Kendall et al., 2017; Stockey et al., 2020).

This study is designed around a novel combination of proxy data including $\delta^{13}\text{C}_{\text{org}}$, $\delta^{15}\text{N}_{\text{bulk}}$, $\delta^{98/95}\text{Mo}$, iron speciation, and minor elements that allows evaluation of changes in nutrient cycling and primary productivity as well as reconstruction of regional bottom water redox conditions. We investigated both intra-shelf basin and slope settings in South China to characterize spatial variability along a depth transect. Moreover, $\delta^{98/95}\text{Mo}$ and Mo concentrations in euxinic sediments and their interrelationships can help to determine the extent of seafloor euxinia. Our data thus allow delineation of the bottom-water redox history of the Middle to Late Ordovician Yangtze Sea, yielding new insights into oceanic changes during this critical time interval and, specifically, into linkages between ocean-redox perturbations and biotic turnover.

2. Geologic setting

The South China Craton was located close to the paleo-Equator during the Middle Ordovician (Fig. 1A), where the mean sea-surface temperature (SST) is estimated to have been $\sim 30^{\circ}\text{C}$ (Trotter et al., 2008). The epicratonic Yangtze Sea was connected to the open ocean along its northern and eastern margins (Fig. 1A). These connections allowed intense upwelling of cold and nutrient-rich intermediate waters, favoring high surface-water productivity (Jin et al., 2018). The Zhenjin section ($31^{\circ}21'12.2''\text{ N}$, $111^{\circ}23'22.9''\text{ E}$) is located in an intra-shelf basin of the Yangtze Platform (Song et al., 2017; Fang et al., 2020) (Fig. 1B). It consists (from the base upward) of biomictic limestone of the Kuniutan Formation, overlain by organic-rich shale of the Miaopo Formation interbedded with thin (<20 cm) but laterally continuous shell-rich limestone layers, and argillaceous limestone of the Pagoda Formation (Fig. 2A). The Darriwilian and Sandbian stages are confidently identified and correlated based on graptolite and conodont biozonations, as previously described in Fang et al. (2020).

The Anye-1 core ($30^{\circ}39'0.1''\text{ N}$, $119^{\circ}30'3.1''\text{ E}$) is located ~ 780 km to the east of the Zhenjin section and ~ 220 km northeast of the Huangnitang section. It represents deeper waters of the Jiangnan Slope far from the shallow carbonate facies of the Yangtze Platform. It consists (from the base upward) of gray shale of the Ningkuo Formation, black shale of the overlying Hulo Formation with a greater siliceous fraction, and argillaceous limestone of the

Yanwashan Formation (Fig. 2B). Several graptolite biozones were identified and correlated to the Huangnitang section, which is the GSSP for the base of the Darriwilian Stage.

3. Methods

3.1. Geochemistry

Fresh and vein-free samples were collected from the Zhenjin section ($n = 17$) and Anye-1 core ($n = 50$), crushed to powder, and prepared for a variety of geochemical analyses. For $\delta^{13}\text{C}_{\text{org}}$ and bulk $\delta^{15}\text{N}$ analyses, powdered samples were first leached and boiled in 3-M HCl to completely remove the carbonate fraction. The residue was then washed in ultrapure water to adjust the pH to 7, collected in a centrifuge tube, and dried overnight. Total organic carbon (TOC) was determined by difference from total C and carbonate C using an ELTRA CS 800 analyzer and reported as weight percent. $\delta^{13}\text{C}_{\text{org}}$ and $\delta^{15}\text{N}_{\text{bulk}}$ analyses were conducted using a Thermo Delta V Advantage MS coupled to a Flash 2000 element analyzer. The isotope values were calibrated and reported in per mil (‰) variation relative to VPDB (for $\delta^{13}\text{C}_{\text{org}}$) and atmospheric N₂ (for $\delta^{15}\text{N}_{\text{bulk}}$). Analytical precision was 0.1‰ for $\delta^{13}\text{C}_{\text{org}}$ and 0.2‰ for $\delta^{15}\text{N}_{\text{bulk}}$. C and N isotopes were analyzed at the Nanjing Institute of Geology and Palaeontology, Chinese Academy of Sciences (NIGPCAS), and China University of Geosciences (CUG)-Wuhan.

Major element oxide data, including Al₂O₃ and Fe₂O₃, were generated by X-ray fluorescence (XRF) spectroscopy, with a precision better than 5%. Trace elements were analyzed using crushed powders digested in HCl-HF-HNO₃ and then measured by inductively coupled mass spectrometry (ICP-MS). Based on duplicate analyses, the accuracy of ICP-MS data was better than 5%, compared with 10% for the XRF data. To evaluate elemental enrichments, trace-metal concentrations are presented as "enrichment factors" (EF), where $X_{\text{EF}} = [(X/\text{Al})_{\text{sample}} / (X/\text{Al})_{\text{PAAS}}]$, and X and Al represent the concentrations of the elements X and Al, respectively. Samples were normalized to the post-Archean average shale (PAAS) compositions of Taylor and McLennan (1985). In addition, excess Ba and P values were calculated as total concentrations minus detrital inputs, i.e., $Ba_{\text{xs}} = Ba_{\text{sample}} - (Ba/\text{Al})_{\text{detr}} \times Al_{\text{sample}}$, and $P_{\text{xs}} = P_{\text{sample}} - (P/\text{Al})_{\text{detr}} \times Al_{\text{sample}}$, where detrital concentrations for average upper continental crust were taken from Taylor and McLennan (1985). All elemental analyses were conducted at the NIGPCAS.

Iron speciation was determined using a standard sequential extraction: sodium acetate to extract iron carbonate minerals (Fe_{carb}), followed by 50 g/L sodium dithionite to extract iron oxides (Fe_{ox}), and 0.2-M ammonium and 0.18-M oxalic acid to extract magnetite (Fe_{mag}) (Poulton and Canfield, 2005). The Cr-reduction method was used to extract pyrite sulfur (Canfield et al., 1986). Pyrite sulfur isotopes were determined by online combustion of Ag₂S produced from extracted pyrite and subsequent analysis by a Delta V isotope ratio mass spectrometer (IRMS). Sulfur isotopes are reported in standard δ -notation as per mil (‰) deviation from VCDT, with an analytical error of $<0.2\text{‰}$. Pyrite iron (Fe_{py}) was calculated from pyrite sulfur content according to the FeS₂ stoichiometry. Total highly reactive iron (Fe_{HR}) was calculated as the sum of the four reactive iron fractions above, i.e., $Fe_{\text{HR}} = Fe_{\text{carb}} + Fe_{\text{ox}} + Fe_{\text{mag}} + Fe_{\text{py}}$. Elevated ratios of highly reactive iron to total iron (i.e., $Fe_{\text{HR}}/Fe_{\text{T}}$) distinguish oxic from suboxic-anoxic facies, with 0.38 as the lower threshold for anoxia, and values of 0.22–0.38 being of ambiguous redox significance. Ratios of pyrite Fe to highly reactive Fe (i.e., $Fe_{\text{py}}/Fe_{\text{HR}}$) >0.7 –0.8 indicate euxinia (i.e., anoxia with sulfidic bottomwaters) when coupled to elevated $Fe_{\text{HR}}/Fe_{\text{T}}$ (Poulton and Canfield, 2005). In contrast, $Fe_{\text{py}}/Fe_{\text{HR}} <0.7$ coupled to elevated $Fe_{\text{HR}}/Fe_{\text{T}}$ ratios suggests ferruginous conditions (i.e., anoxic

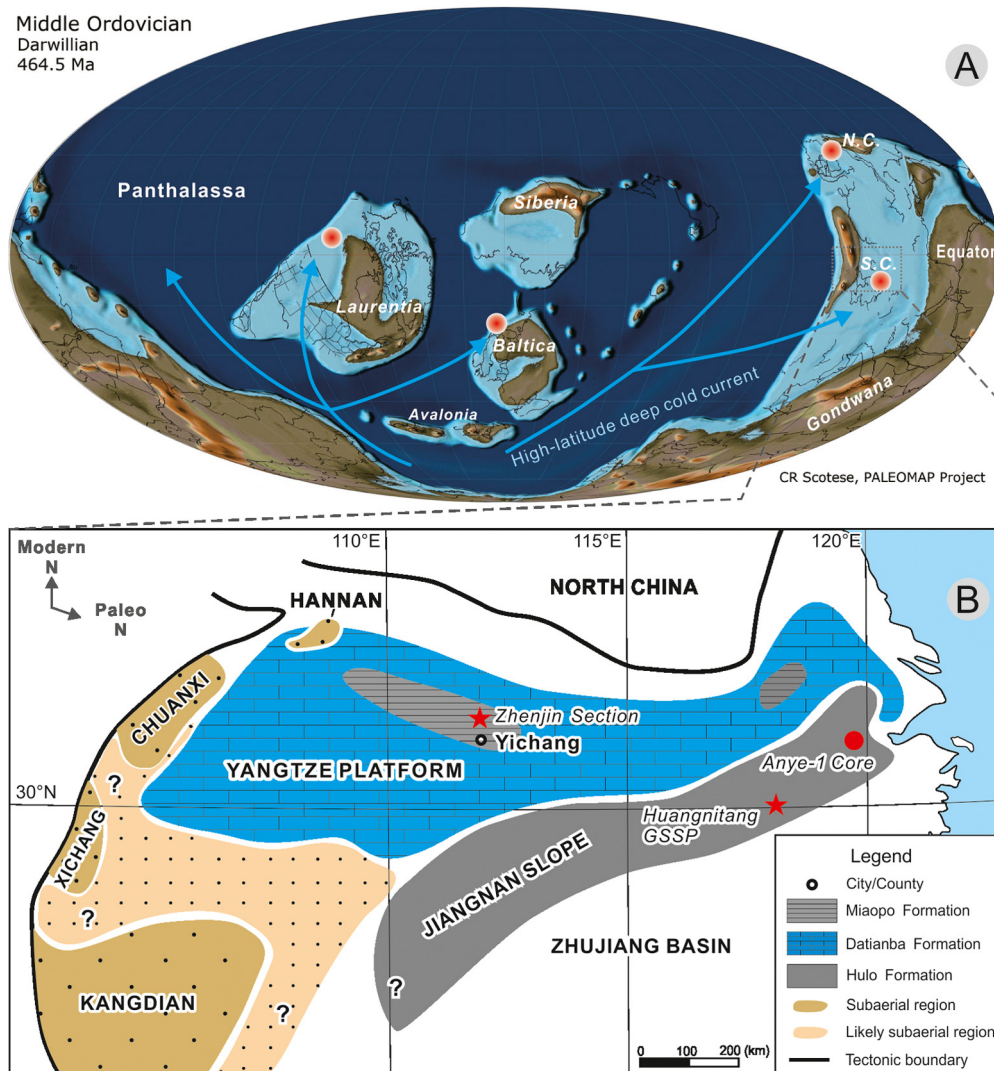


Fig. 1. (A) Global paleogeography of Middle Ordovician, after Scotese (2014) and Jin et al. (2018). S.C. = South China; N.C. = North China. Purple symbols represent black shales recovered from Ordovician anoxic (euxinic) basins in different continents, including the Ningkuo and Hulo shales (South China), the Wulalike shale (North China), the Alum Shale (Sweden), and the Road River Group (Yukon, Canada). (B) Paleoenvironmental map showing the location of the two study sites on the South China Craton and their depositional environments; modified from Fang et al. (2020). The Huangnitang section is the GSSP (Global Boundary Stratotype Section and Point) for the base of the Darriwilian Stage. (For interpretation of the colors in the figure(s), the reader is referred to the web version of this article.)

and iron-rich). The sulfur isotope and Fe speciation data were generated at the State Key Laboratory of Biogeology and Environmental Geology (BGEG) at CUG-Wuhan.

After determination of Mo concentrations, samples containing >100 ng Mo were prepared for Mo isotope analysis by oxidizing an aliquot of powder at 600°C for 8 h and transferring the product to a breaker. The sample was then digested in a mixture of HF and HNO_3 (1:2) at 100°C for more than 6 h, yielding complete dissolution. An anion/cation exchange resin/double-column procedure was used to separate Mo from the sample. Samples were introduced to the MC-ICP-MS using a cyclonic chamber system with a PFA pneumatic nebulizer in the free aspiration mode. All samples and reference solutions were run in two blocks of 15 cycles of measurement. After each run, the nebulizer and spray chamber were rinsed with 0.6-M HNO_3 to maintain signal intensity at the original background level. To eliminate possible dilution, concentrations of samples and a bracketing Mo reference (NIST SRM 3134) were matched to within 10%. The $\delta^{98/95}\text{Mo}$ results for the reference standard can be found in Table S2 in Supple-

mentary material. Calculating $\delta^{98/95}\text{Mo}$ relative to NIST SRM 3134 was achieved by setting the $\delta^{98/95}\text{Mo}$ of NIST SRM 3134 at $+0.25\text{\textperthousand}$ (Nägler et al., 2014) as follows:

$$\delta^{98/95}\text{Mo}(\text{\textperthousand}) = [(\text{sample}/\text{NIST3134})^{98/95} - 1] \times 1000 \quad (1)$$

The samples for Mo isotope analysis were prepared at Tongwei Technology LTD and then analyzed at the Guangzhou Institute of Geochemistry, Chinese Academy of Sciences.

3.2. Modeling

Our model for the oceanic Mo cycle is based on mass-balance calculations:

$$\text{dM/dt} = F_{\text{riv}} - F_{\text{ox}} - F_{\text{SAD}} - F_{\text{eux}} \quad (2)$$

where 'M' denotes the oceanic Mo reservoir and 'F' represents the source flux related to rivers (riv), and the sink fluxes linked to burial in oxic facies (ox), sulfides at depth (SAD), and euxinic facies

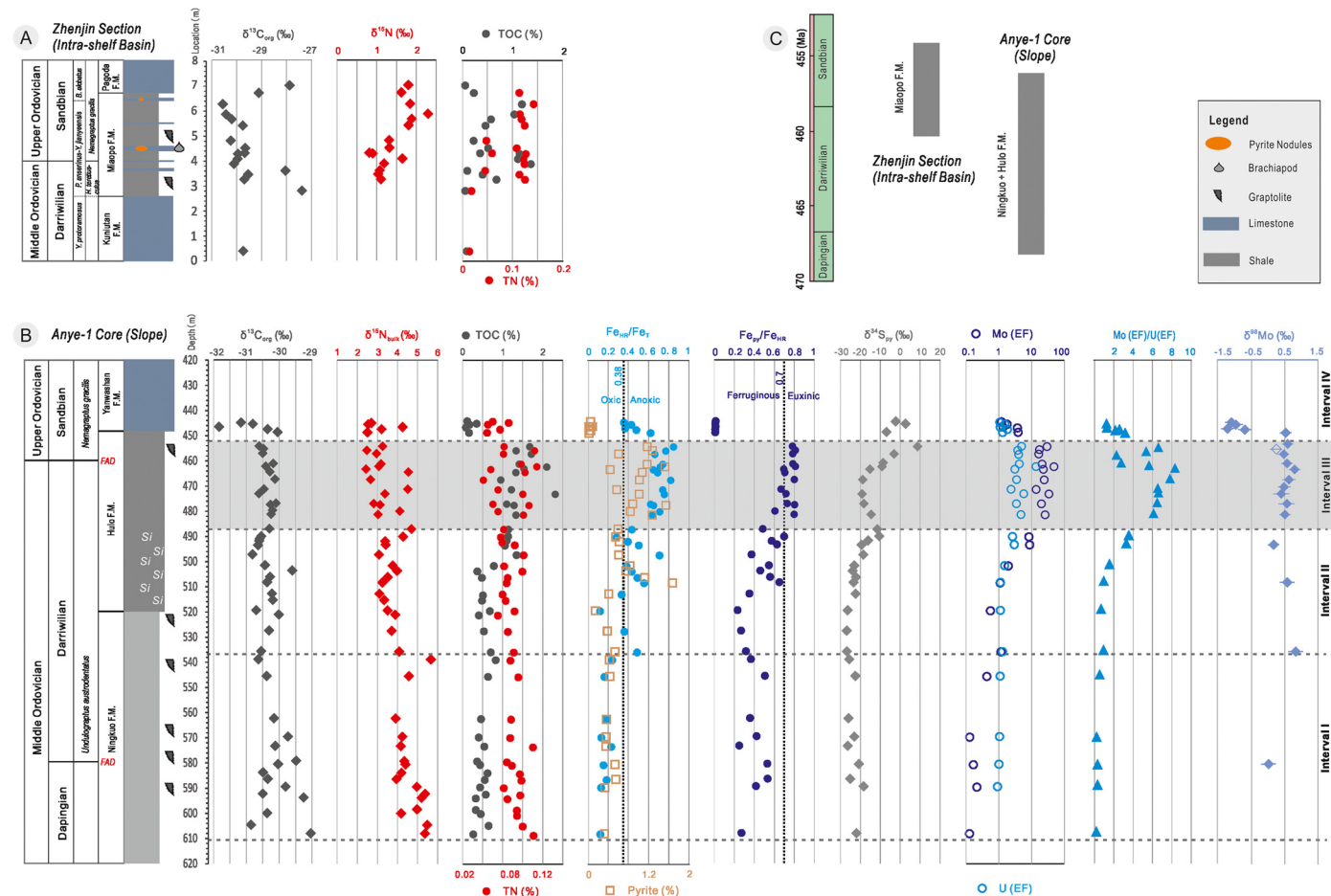


Fig. 2. Geochemical profiles for the Zhenjin outcrop section (A) and Anye-1 core (B), and geochronologic ranges of the two study sections (C). Dotted lines in the iron speciation columns represent thresholds for anoxic and euxinic facies (from Poulton and Canfield, 2005). The gray shaded field represents the euxinic Interval III inferred from iron-speciation and trace-metal data. "Si" in the lithology column represents siliceous components in the shale, with no nodule or thick bed found.

(eux). The SAD sink represents a substantial proportion of Mo removal that occurs under less intensely reducing conditions, neither in fully oxic nor in fully euxinic systems, thus with Mo concentrations typically lower than 25 ppm (Scott and Lyons, 2012; Kendall et al., 2017).

The isotopic composition of Mo in seawater (sw) can be calculated as:

$$\delta^{98/95}\text{Mo}_{\text{SW}} = \delta_{\text{riv}} + f_{\text{ox}}\Delta_{\text{ox}} + f_{\text{SAD}}\Delta_{\text{SAD}} + f_{\text{eux}}\Delta_{\text{eux}} \quad (3)$$

where $\delta^{98/95}\text{Mo}_{\text{SW}}$ is the seawater Mo-isotopic composition; δ_{riv} is the isotopic composition of rivers; Δ denotes isotopic fractionations associated with the oxic, SAD, and euxinic sinks; and f denotes the relative proportions of Mo removed to oxic, SAD, and euxinic facies. We assumed that the oceanic Mo cycle was in an initial steady state in each modeling scenario, and that $\delta_{\text{riv}} = 0.3\text{\textperthousand}$, $\Delta_{\text{ox}} = 2.8\text{\textperthousand}$, $\Delta_{\text{SAD}} = 0.8\text{\textperthousand}$, and $\Delta_{\text{eux}} = 0.3\text{\textperthousand}$ (Dahl et al., 2010; Kendall et al., 2017; Stockey et al., 2020; Gill et al., 2021). These parameters are reasonably set to reproduce the low $\delta^{98/95}\text{Mo}_{\text{SW}}$ values previously estimated for Ordovician seawater (Dahl et al., 2010).

4. Results

The Anye-1 core shows higher TOC contents ($0.8\% \pm 0.06\%$) and lower TN ($0.07\% \pm 0.004\%$) than the Zhenjin section (TOC $0.6\% \pm 0.02\%$, TN $0.09\% \pm 0.007\%$) (Table S1 in Supplementary material). Zhenjin yielded $\delta^{13}\text{C}_{\text{org}}$ values ranging from $-30.6\text{\textperthousand}$ to $-27.4\text{\textperthousand}$

(Fig. 2A). These data, when combined with published $\delta^{13}\text{C}_{\text{carb}}$ profiles for other sections (Kah et al., 2016), can be used to correlate the study sections with those distributed globally. The Anye-1 core yielded relatively lower $\delta^{13}\text{C}_{\text{org}}$ values, mostly varying between $-31.8\text{\textperthousand}$ and $-28.8\text{\textperthousand}$ (Fig. 2B). Recognition of the MDICE from the organic isotope profiles is not straightforward unless combined with well-established graptolite biozonations for the study sections. $\delta^{15}\text{N}_{\text{bulk}}$ varies between $+0.8\text{\textperthousand}$ and $+2.3\text{\textperthousand}$ at Zhenjin and between $+2.4$ and $+5.6\text{\textperthousand}$ in the Anye-1 core, both showing a negative shift of $\sim -3\text{\textperthousand}$ from the early Darriwilian to Sandbian (Fig. 2B).

For the Anye-1 core, low ratios of $\text{Fe}_{\text{HR}}/\text{Fe}_T$ (mean: 0.18) and $\text{Fe}_{\text{py}}/\text{Fe}_{\text{HR}}$ (mean: 0.42) suggest oxic bottom waters during the late Dapingian to earliest Darriwilian. $\delta^{34}\text{S}_{\text{py}}$ values for the oxic interval (Interval I, drill core depth 610–538 m) are also low ($\sim -23\text{\textperthousand}$) (Fig. 2B). Values of $\text{Fe}_{\text{HR}}/\text{Fe}_T$ in the shale-dominated portion of the core increase upwards (mean: 0.46), suggesting a change in benthic redox state from oxic to ferruginous conditions during the early to mid-Darriwilian (Interval II, depth 538–488 m) in parallel with a shift in $\delta^{34}\text{S}_{\text{py}}$ to higher values ($-11.5\text{\textperthousand}$) (Fig. 2B). The shale of the late Darriwilian (Interval III, depth 488–452 m) yields higher $\text{Fe}_{\text{HR}}/\text{Fe}_T$ (mean: 0.72), $\text{Fe}_{\text{py}}/\text{Fe}_{\text{HR}}$ (mean: 0.76), and $\delta^{34}\text{S}_{\text{py}}$ ($\sim -3.0\text{\textperthousand}$), implying euxinic bottom-water conditions. Limestone of Sandbian age in the Anye-1 core (with $\text{Fe}_T > 0.5\%$) shows low $\text{Fe}_{\text{HR}}/\text{Fe}_T$ and $\text{Fe}_{\text{py}}/\text{Fe}_{\text{HR}}$ values, recording a return of redox conditions from sulfidic to oxic (Fig. 2B). Redox-sensitive trace metals such as Mo and U are moderately enriched in the ferruginous (Interval II) and euxinic (Interval III) portions of the Anye-1 core but

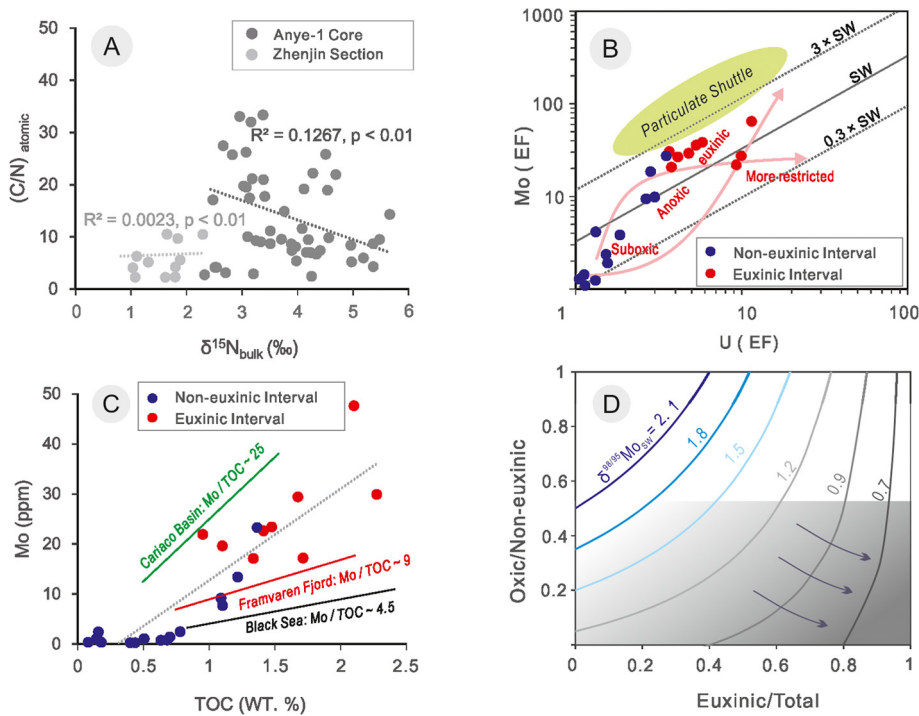


Fig. 3. Geochemical crossplots. (A) C/N(atomic) versus $\delta^{15}\text{N}_{\text{bulk}}$ for both the Zhenjin section and Anye-1 core; the lack of correlation suggests weak diagenetic influence on the N-bearing fraction; (B) Mo versus U enrichment factors for the Anye-1 core; the trajectory suggests weak operation of a particulate shuttle within a semi-restricted basin (cf. Algeo and Tribovillard, 2009); (C) Mo versus TOC of Anye-1 core, with Mo/TOC values of $\sim 10\text{--}20$ indicative of moderate watermass restriction (Algeo and Rowe, 2012); assignment of samples to non-euxinic versus euxinic facies is based mainly on iron speciation data; note that only data with TOC $> 1\%$ and Mo > 10 ppm were included to calculate the slope; (D) Modeling of seawater $\delta^{98}/^{95}\text{Mo}$ as a function of oxic/non-euxinic versus euxinic sink fluxes; the shaded area at bottom right denotes values of $\delta^{98}/^{95}\text{Mo}_{\text{sw}}$ consistent with dominance of sulfidic sinks, whereas the white areas represent unlikely states according to previous interpretations (Dahl et al., 2010; Gill et al., 2021).

less so for the oxic portions (Interval I, 610–538 m; and Interval IV, 452–440 m) (Fig. 2B). Marine $\delta^{98}/^{95}\text{Mo}$ data generated for oxic Interval IV are mostly negative (minimum: $-1.1\text{\textperthousand}$), whereas those for the ferruginous Interval II and euxinic Interval III are relatively more positive (mean: $\sim +0.5\text{\textperthousand}$, maximum: $+0.8\text{\textperthousand}$) (Table S1 in Supplementary material).

5. Discussion

5.1. Nutrient cycling and primary productivity

Nitrogen isotope data for sedimentary rocks have the potential to record past changes in nutrient cycling, primary production, marine redox structure and global climate (Prokopenko et al., 2006; Higgins et al., 2012; Algeo et al., 2014). However, the reliability of this approach has been challenged due to diagenetic effects that can alter the N isotope composition of organic matter, including selective degradation of amino acids and deamination during aerobic bacterial decomposition of organic matter (Loureys et al., 2003). The former process preferentially removes ^{15}N -enriched protein, resulting in lower $\delta^{15}\text{N}$ values and higher C/N atomic ratios in the sediment (Junium and Arthur, 2007), whereas the latter process releases isotopically light NH_4^+ that, if lost to upward diffusion, leaves an isotopically heavy residue in the sediment (Prokopenko et al., 2006). However, if NH_4^+ produced within the sediment is captured by clay minerals, the bulk sediment generally shows little or no change in $\delta^{15}\text{N}$ relative to the organic sinking flux (Higgins et al., 2012). As such, bulk N measurements have the potential to capture primary $\delta^{15}\text{N}$ values through incorporation of liberated organic N retained in clay minerals (Higgins et al., 2012). Both of the investigated sections yield low C/N(atomic) ratios and moderate $\delta^{15}\text{N}$ values (Fig. 3A), with no linear correlation between these proxies ($R^2 = 0.002$ for Zhenjin section and 0.127 for Anye-1 core).

Low C/N(atomic) (mostly < 30) and poor correlation with $\delta^{15}\text{N}$ suggest that bulk $\delta^{15}\text{N}$ has not been significantly altered by early diagenesis (Junium and Arthur, 2007) and is thus a reliable record of primary marine $\delta^{15}\text{N}$ (i.e., the isotopic composition of bioavailable seawater nitrogen).

At Zhenjin, $\delta^{15}\text{N}_{\text{bulk}}$ values are low (mainly 0 to $+2\text{\textperthousand}$), which is close to the $\delta^{15}\text{N}$ of atmospheric N_2 ($\sim 0\text{\textperthousand}$) and significantly below the average for modern oceanic sediments ($\sim +5\text{\textperthousand}$). This observation suggests that microbial N-fixation was the main source of biologically available nitrogen within the intra-shelf basin (Fig. 2A). Previous studies have ascribed dominance of nitrogen fixation to large-scale removal of oceanic fixed nitrogen via denitrification and ammonia oxidation, especially in stratified and anoxic basins (Junium and Arthur, 2007; Algeo et al., 2014). Moreover, redox proxies such as iron speciation and trace elements argue for dysoxic conditions of bottom waters at Zhenjin, implying enhanced denitrification in the sediment column. The inferred presence of some oxygen is consistent with the occurrence of abundant benthic fossils in that section (Fang et al., 2020). High accumulation rates of excess Ba and P suggest that moderate to high productivity was prevalent throughout the late Darriwilian (cf. Fang et al., 2020). Moreover, the rise of $\delta^{15}\text{N}_{\text{bulk}}$ from $+0.8\text{\textperthousand}$ to $+2.3\text{\textperthousand}$ suggests a modest decrease in the contribution of microbial N-fixation to total biologically available nitrogen in the surface ocean during the Sandbian, perhaps reflecting episodic deep-water oxygenation (Kozik et al., 2019; Fang et al., 2020).

At Anye-1, the $\delta^{15}\text{N}_{\text{bulk}}$ record shows a secular negative shift of about 3\textperthousand that extends over the entire study interval (Fig. 2B). Higher $\delta^{15}\text{N}_{\text{bulk}}$ values (mean $+4.7\text{\textperthousand}$) in the upper Dapingian to lowermost Darriwilian are close to the $\delta^{15}\text{N}$ of modern marine sediments, reflecting an oxygenated mode of operation for the nitrogen cycle at that time (cf. Prokopenko et al., 2006; Algeo et al., 2014). A subsequent negative $\delta^{15}\text{N}_{\text{bulk}}$ excursion through the lower

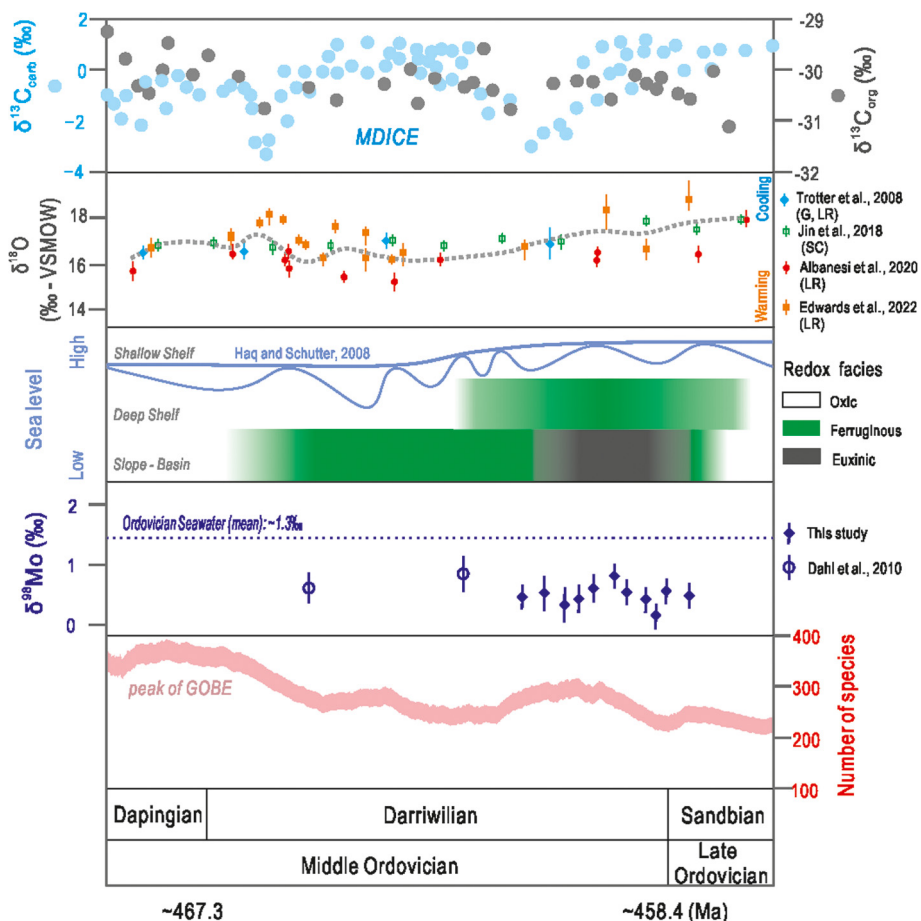


Fig. 4. The environmental framework for biotic turnover following the peak of GOBE, including carbon cycle, fossil $\delta^{18}\text{O}$, marine redox structure and evolution of the Yangtze Sea, and species diversity changes. Carbonate carbon isotopes are from Kah et al. (2016) and Young et al. (2016), and organic carbon isotopes are from this study. The redox facies were assigned mainly on the basis of iron speciation data from Fang et al. (2020) and this study. The species diversity curve is modified from Deng et al. (2021). Black shales yield a mean $\delta^{98/95}\text{Mo}$ for Ordovician seawater of $\sim +1.3\text{\textperthousand}$ (Dahl et al., 2010). G = Gondwana; LR = Laurentia; SC = South China (Albanesi et al., 2020; Edwards et al., 2022; Haq and Schutter, 2008).

Darriwilian to lower Sandbian implies that the contribution of microbial N-fixation to the bioavailable nitrogen supply increased. This pattern is typical of regions characterized by benthic anoxia related to enhanced primary production and organic matter export (Lourety et al., 2003; Ader et al., 2014), as in parts of the modern eastern Pacific in which elevated productivity is indicated by excess Ba and P accumulation rates (Schoepfer et al., 2015; Fang et al., 2020). Barium and P evidence of moderate to high productivity in the surface waters of the Ordovician Yangtze Sea (see above) thus supports our inference of enhanced microbial N fixation. However, $\delta^{15}\text{N}$ did not decline below 0\textperthousand , suggesting a lack of photic-zone euxinia during the study interval, in contrast to conditions during some ancient oceanic anoxic events and in modern anoxic basins (Prokopenko et al., 2006; Higgins et al., 2012). Persistence of low $\delta^{15}\text{N}_{\text{bulk}}$ ($\sim +2\text{\textperthousand}$) into the oxic Interval IV (452–440 m) may have been caused by established patterns of ecosystem utilization of bioavailable nitrogen, reflecting a delayed response of the nitrogen cycle to the abrupt marine redox change from dysoxic to oxic conditions.

The different patterns of $\delta^{15}\text{N}_{\text{bulk}}$ variation in intra-shelf basin (Zhenjin) and slope (Anye-1) settings of the Yangtze Platform reflect spatial variability in the marine nitrogen cycle, probably due to local influences on primary production and watermass redox structure (cf. Ader et al., 2014; Algeo et al., 2014). The decline in $\delta^{15}\text{N}_{\text{bulk}}$ values (from $\sim +5.5\text{\textperthousand}$ to $\sim +2\text{\textperthousand}$) at the slope site may record the dynamic expansion of anoxic intermediate-depth waters during the late Middle Ordovician. Large negative shifts in

sediment $\delta^{15}\text{N}$ can also be triggered by intensified upwelling from intermediate depths (~ 200 – 1000 m), enhancing ammonium assimilation, as proposed for OAE2 (Junium and Arthur, 2007; Higgins et al., 2012). However, very low $\delta^{15}\text{N}$ values (i.e., $< 0\text{\textperthousand}$) have not been reported for the slope belt of the Yangtze Sea, which implies that the nitrogen cycle operated in at least semi-oxygenated waters (Prokopenko et al., 2006; Algeo et al., 2014).

5.2. Expansion of marine anoxia in the Yangtze Sea

The secular evolution of ancient marine redox conditions can be reconstructed using iron speciation and redox-sensitive trace-metal data (e.g., Poulton et al., 2004; Sperling et al., 2021). A combination of reactive iron and redox-sensitive trace-element data are used here to better constrain the benthic redox history of the Yangtze Sea during the Middle to Late Ordovician.

The intra-shelf basin in which the Zhenjin section is located experienced dysoxic bottom-water conditions during the late Darriwilian to early Sandbian, as evidenced by intermediate $\text{Fe}_{\text{HR}}/\text{FeT}$ values and low abundances of pyrite and redox-sensitive trace metals such as Mo and U (cf. Fang et al., 2020). However, its redox state was episodically perturbed by deep-water oxygenation events, as evidenced by the occurrence of shelly fossils (e.g., brachiopods) and bioturbation structures in thin-bedded (< 5 cm) limestone (Song et al., 2017).

The slope of the Yangtze Platform reveals a more complicated redox history than the platform's intra-shelf basin. Low $\text{Fe}_{\text{HR}}/\text{FeT}$

and $\text{Fe}_{\text{py}}/\text{Fe}_{\text{HR}}$ ratios at Anye-1 indicate that local bottom waters were predominantly oxic from the late Dapingian to the early Darriwilian (Interval I). As the redox boundary was within the sediment, the concentrations of trace metals such as Mo and U were quite low and similar to those of modern sediments in oxygenated marginal-marine environments (Algeo and Tribovillard, 2009). Subsequently, during the early to mid-Darriwilian (Interval II), ferruginous waters developed gradually on the slope. Under these conditions, the limited availability of sulfide caused less molybdenum to accumulate relative to uranium, as reflected by their relative enrichment factors. The Anye-1 core exhibits a corresponding positive shift of pyrite $\delta^{34}\text{S}$, progressively from $-26.8\text{\textperthousand}$ to $-11.5\text{\textperthousand}$ (Fig. 2B), suggesting an increase in microbial sulfate reduction and pyrite burial in the Yangtze Sea during the MDICE (Interval II). That possibility is also consistent with concurrent positive excursions of $\delta^{13}\text{C}_{\text{carb}}$ ($\sim 2\text{\textperthousand}$), $\delta^{34}\text{S}_{\text{CAS}}$ and $\delta^{34}\text{S}_{\text{Py}}$ ($\sim 10\text{-}15\text{\textperthousand}$) in carbonate platform settings (Young et al., 2016), under the scenario of a combination of increased productivity in the ocean-surface layer and expanded seafloor anoxia. The existence of more reducing (even euxinic) bottom waters on the slope of the Yangtze Platform is supported by large enrichments of sedimentary pyrite and Mo (Fig. 2B). The covariation pattern of Mo and U also reveals relatively enhanced Mo uptake (Fig. 3B), consistent with weak operation of a particulate shuttle, which tends to operate under fluctuating redox conditions (Algeo and Tribovillard, 2009; Goldberg et al., 2012). At the same time, an increase in the intensity of microbial sulfate reduction induced a large shift ($\sim +27\text{\textperthousand}$) in $\delta^{34}\text{S}_{\text{Py}}$ (Interval III in Fig. 2B). Although such perturbations of the sulfur cycle recorded by pyrite $\delta^{34}\text{S}$ may be influenced by local effects such as sedimentation rate and organic matter and reactive Fe contents in sediments (Lang et al., 2020), they record enhanced pyrite burial under strongly reducing conditions in intermediate waters of the Yangtze Sea. Therefore, we can propose a progressive expansion of marine anoxia along the slope of Yangtze Sea during the Darriwilian. The development of seafloor euxinia in the late Darriwilian oceans was likely significant but not persistent due to subsequent oxygenation events driven by enhanced ventilation.

5.3. The extent of global seafloor euxinia

To explore changes in the extent of marine euxinia during the late Darriwilian, we generated $\delta^{98/95}\text{Mo}$ data for the black shale succession that accumulated on the Yangtze Platform slope (Fig. 2B). $\delta^{98/95}\text{Mo}$ in organic-rich mudstones has been used as a proxy to track global changes in seawater Mo isotopes during the Precambrian and Paleozoic, linked to the general oxygenation state of the atmospheric-oceanic system (Dahl et al., 2010; Kendall et al., 2017). However, caution must be exercised in interpreting sediment $\delta^{98/95}\text{Mo}$ data, which can be primarily controlled by the redox state of local bottom waters under certain conditions (Nägler et al., 2005; Goldberg et al., 2012; Noordmann et al., 2015). Indeed, distinguishing Mo isotope fractionation associated with local basinal versus global-ocean redox controls remains problematic unless combined with other proxies such as sedimentary iron speciation and redox-sensitive metal data to test local environmental redox conditions (Kendall et al., 2017; Gill et al., 2021).

The Mo isotope composition of contemporaneous seawater can be captured by the sediment if aqueous Mo is drawn down quantitatively in a highly restricted and euxinic marginal-marine basin (Dahl et al., 2010; Kendall et al., 2017). The molybdenum reservoir of a restricted basin will be Mo-depleted and induce low Mo/TOC in the sediment (Algeo and Rowe, 2012). The $\delta^{98/95}\text{Mo}$ profile for the Anye-1 core exhibits moderate values for the euxinic interval (Interval III, mean $+0.5\text{\textperthousand}$, peak $+0.8\text{\textperthousand}$) that are similar to those previously reported for Middle Ordovician euxinic shales ($\sim +0.6\text{\textperthousand}$) and lower than the inferred $\delta^{98/95}\text{Mo}$ of Early Paleo-

zoic seawater $\delta^{98/95}\text{Mo}$ ($\sim +1.3\text{\textperthousand}$; Dahl et al., 2010). The Anye-1 core yields moderate Mo/TOC ratios (~ 18 ; Fig. 3C), suggesting that the watermass was only moderately restricted, comparable to the degree of restriction of the modern Framvaren Fjord and Cariaco Basin (Algeo and Rowe, 2012). In such settings, higher Mo/TOC ratios indicate more frequent deepwater renewal, enhanced Mo resupply, and possibly lower sulfide concentrations (Algeo and Rowe, 2012; Gill et al., 2021). The removal of Mo from seawater via absorption to Fe-Mn nodules and hydrothermal Mn crusts yields a large equilibrium isotope fractionation of $\sim -3\text{\textperthousand}$, producing an offset between the $\delta^{98/95}\text{Mo}$ of organic-rich sediments and the seawater source (Nägler et al., 2005; Goldberg et al., 2012). In the present study units, the covariation pattern of Mo_{EF} and U_{EF} (Fig. 3B) implies possible operation of a particulate shuttle in a redox environment that fluctuated from oxic to euxinic (cf. Algeo and Tribovillard, 2009). The existence of a particulate shuttle may have contributed to the observed low $\delta^{98/95}\text{Mo}$ values (even for euxinic Interval III) as a local control via Mn-redox cycling (Goldberg et al., 2012; Noordmann et al., 2015; Cheng et al., 2016). However, the expected correlation does not exist between the ratios of Mo/U enrichment and $\delta^{98/95}\text{Mo}$ for the euxinic shale (Fig. 2B), suggesting limited influences of local Mn-redox variations on sediment $\delta^{98/95}\text{Mo}$ during euxinic Interval III.

Strongly euxinic mudstones can yield high $\delta^{98/95}\text{Mo}$ ($> +2\text{\textperthousand}$) and Mo concentrations ($> 100 \text{ ppm}$) (Scott and Lyons, 2012). However, a wide range of moderate $\delta^{98/95}\text{Mo}$ can be observed for euxinic sediments when the overlying bottom waters are intermittently euxinic or contain low $[\text{H}_2\text{S}]_{\text{aq}} < 11 \mu\text{M}$, which determines whether Mo can be quantitatively removed from sulfidic bottom waters to the sediment and whether intermediate thiomolybdate species and their associated fractionations persist (Nägler et al., 2005; Scott and Lyons, 2012; Kendall et al., 2017). Such weakly euxinic conditions with low and fluctuating sulfide concentrations are common in less restricted continental margin basins, where the sediments are also characterized by lower $\delta^{98/95}\text{Mo}$ and modest Mo concentrations (Scott and Lyons, 2012; Cheng et al., 2016). In this study, low $\delta^{98/95}\text{Mo}$ and moderate Mo concentrations for the euxinic Interval III of the Anye-1 core may suggest weakly euxinic conditions of bottom waters along the slope of the Yangtze Platform. Such weakly euxinic bottom waters with fluctuating availability of dissolved H_2S for the Mo removal is likely due to periodic deep-water oxygenation, as oceanic ventilation was enhanced following the long-term cooling and increased atmospheric oxygenation (Kah et al., 2016; Edwards et al., 2017).

Earlier, during deposition of the predominantly ferruginous Interval II, the mid-Darriwilian shale equivalent to the MDICE horizon shows a rise of $\delta^{98/95}\text{Mo}$ from $\sim 0\text{\textperthousand}$ to $+0.8\text{\textperthousand}$ followed by a slow fall to $+0.2\text{\textperthousand}$ (Fig. 2). Such variation may have resulted from local variations in the degree of non-quantitative versus quantitative uptake of Mo, possibly related to shifts between ferruginous (lower $\delta^{98/95}\text{Mo}$) and weakly euxinic conditions (higher $\delta^{98/95}\text{Mo}$). Rather negative $\delta^{98/95}\text{Mo}$ values ($< -0.5\text{\textperthousand}$) are present in argillaceous limestone at the base of the Yanwashan Formation (Interval IV). This large offset from seawater $\delta^{98/95}\text{Mo}$ could reflect a local change to nearly oxic bottom-water conditions, which is supported by markedly lower concentrations of redox-sensitive metals in Interval IV (Fig. 2) (Nägler et al., 2005; Goldberg et al., 2012).

The $\delta^{98/95}\text{Mo}$ values for the euxinic Interval IV of the Anye-1 core are comparable to previously published values for Ordovician black shales (Dahl et al., 2010). Assuming $\delta^{98/95}\text{Mo}$ of euxinic shales has the potential to track the isotopic composition of global seawater, estimated lower $\delta^{98/95}\text{Mo}_{\text{sw}}$ ($< +1.3\text{\textperthousand}$) and the negative shift of $\delta^{98/95}\text{Mo}$ from $+0.8\text{\textperthousand}$ to $+0.4\text{\textperthousand}$ during Interval IV would indicate an increase in the euxinic and/or the SAD sinks at the expense of oxic sinks for molybdenum. Our modeling plot (Fig. 3D) shows that the shift of $\delta^{98/95}\text{Mo}$ to more negative con-

tours requires the expansion of seafloor euxinia in the oceans to facilitate predominantly sulfidic sinks for Mo removal. In such scenarios, low $\delta^{98/95}\text{Mo}$ can be achieved for euxinic sediments even without the increase in SAD sinks. That possibility may also imply that the ocean was not such oxygenated (at least) during the Middle-Late Ordovician, which is also suggested by long-term calibration of oceanic redox with carbonate proxies such as cerium anomalies and iodine abundances (Wallace et al., 2017; Lu et al., 2018).

The general trend in the global ocean during the Ordovician is thought to have been toward more oxidizing conditions in step with the rise of atmospheric oxygen (Edwards et al., 2017). Moreover, an inferred decrease in the seawater $\delta^{34}\text{S}$ during the middle-late Darriwilian that was decoupled from the $\delta^{13}\text{C}_{\text{carb}}$ record has been ascribed to a decline of pyrite burial rates due to increased oceanic ventilation (Young et al., 2016). Further, enhanced oceanic ventilation may have caused partial oxidation of a deep-water HS⁻ reservoir, leading to a reorganization of the sulfur cycle during the Middle Ordovician (Kah et al., 2016). However, the prolonged expansion of marine anoxia on the Yangtze Platform slope in the late Darriwilian (this study), as well as contemporaneous expansion of marine anoxia in some other epicontinental seas (Kozik et al., 2019), seems inconsistent with interpretations of increased oceanic oxygenation driven by enhanced ventilation and a rise of atmospheric O₂ levels in response to global cooling (Young et al., 2016; Edwards et al., 2017).

Notably, such shifts in spatially variable redox must be understood in the context of the localized effects of global cooling. Long-term cooling during the Middle to Late Ordovician (Trotter et al., 2008) may have resulted in generally invigorated oceanic circulation, widely ventilating deep-ocean regions. At the same time, enhanced oceanic circulation also led to intensified upwelling on some continental margins and basins (Marlow et al., 2000), further stimulating surface-water productivity and organic carbon sinking fluxes, resulting in locally more reducing benthic conditions. We infer that the Yangtze Platform was located in such an upwelling zone, and that it is likely to have been in a less oxygenated ocean during the Middle and Late Ordovician (Dahl et al., 2010; Wallace et al., 2017; Sperling et al., 2021). However, links between upwelling intensity and climate change can be spatially complex. Further research, including quantitative simulations, will be needed to better constrain these relationships for the Ordovician ocean.

5.4. Implications for Middle-Late Ordovician biotic turnover

As a milestone of biodiversification in the early Paleozoic, the GOBE achieved its peak in the mid-Middle Ordovician, followed by a decline in the diversity of marine invertebrates during the late Middle to Late Ordovician (Servais et al., 2010; Fan et al., 2020). Statistical analysis of fossil records reveals a ~15-Myr interval (corresponding to the Darriwilian to Sandbian stages) characterized by a 40% decrease in species biodiversity globally, with a 56% decline for benthic species in South China (Fig. 4) (Deng et al., 2021). Although the peak of GOBE in South China was in the early Darriwilian and much earlier than the peaks in Laurentia and Baltica, the falling trend seems to have appeared before the early Sandbian (Servais and Harper, 2018). However, no convincing trigger has yet been proposed for this abrupt and significant change in marine ecosystems.

The Darriwilian to early Sandbian interval experienced significant perturbations in oceanic redox conditions, as reflected by shifts in the oceanic carbon and sulfur cycles (Kah et al., 2016; Kozik et al., 2019). Despite increased atmospheric oxygenation and oceanic ventilation, bottom-water anoxia of varying lateral extent and duration still existed in various environments and regions (Edwards et al., 2017; Chen et al., 2020; Kozik et al., 2019). Our

findings have identified an expansion of marine anoxia along the slope of Yangtze Platform during the interval of interest, particularly transient bottom-water euxinia in the late Darriwilian (Fig. 4). Similarly, Fe speciation applied to marine shales from a continental basin in Laurentia also reveals persistent anoxia (or euxinia) in deep waters during the Ordovician, with an abrupt increase in authigenic enrichments of Mo relative to U also identified for the late Darriwilian (Sperling et al., 2021). Thus, such progressive expansion of marine anoxia has the potential to be linked to the decrease in species of marine animals according to the temporal consistency in the Yangtze Sea. Specifically, anoxic waters along the slope limited the habitability of deep waters and may have impacted marine communities in shelf areas through upwelling events or chemocline upward excursions. Such occasions have been inferred for several extinction events during the Late Cambrian, Early Ordovician and Early Silurian accompanied by climatic changes (Zhang et al., 2021).

One possibility that must be considered is that the link between redox and biotic changes may represent an “incidental correlation”, and that both anoxia and species decline were probably responding to a third fundamental variable. Another obvious candidate is temperature change, especially cooling, which is considered to have played a major role in many biocrises in Earth history (e.g., Saure et al., 2020). A sharp temperature fall as documented by fossil $\delta^{18}\text{O}$ during the Darriwilian to early Sandbian (Fig. 4) could account for both marine anoxia (through intensification of upwelling, as inferred for the Yangtze Platform, Richardson Trough, and Selwyn Basin) and concurrent species decline. Although specific mechanisms for these extinction events require further investigation, we have provided a testable hypothesis for the drivers of biotic turnover following the peak of the GOBE.

6. Conclusions

A novel combination of geochemical approaches revealed the change in the pattern of nutrient cycling under moderate-high primary productivity, and spatiotemporal variety in the redox landscape from shallow to deep environments in the Yangtze Sea. Moderate $\delta^{98/95}\text{Mo}$ for the euxinic black shale, when modeling points to the presence of seafloor euxinia in the late Darriwilian oceans. Anoxic seafloor may have developed in a less oxygenated ocean and resulted from increased upwelling into continental basins in the aftermath of stepwise Ordovician cooling. Thus, the progressive expansion of bottom-water anoxia in the Yangtze Sea along with seawater temperature decline, can be linked to a significant decline in species of marine animals (especially in South China) following the peak of GOBE. Thus, our findings elucidated potential triggers and mechanisms for the biotic turnover during the Middle-Late Ordovician which denotes the onset of decreasing stage for the GOBE. Future studies should seek additional evidence from different environments on other continents, to further confirm the extent of such a biotic calamity.

CRediT authorship contribution statement

Junpeng Zhang: Conceptualization, Funding acquisition, Investigation, Project administration, Visualization, Writing – original draft, review & editing.

Chao Li, Xiang Fang, and Wenjie Li: Sampling, Investigation, Analyses, Writing – review & editing. **Yiying Deng:** Biodiversity Data Analysis.

Chenyi Tu: Investigation, Writing – review & editing.

Thomas J. Algeo: Conceptualization, Writing – review & editing.

Timothy W. Lyons: Conceptualization, Supervision, Funding acquisition, Writing – review & editing.

Yuandong Zhang: Conceptualization, Funding acquisition, Writing – review & editing.

Declaration of competing interest

The authors declare that they have no known competing financial interests or personal relationships that could have appeared to influence the work reported in this paper.

Data availability

All the data have been included in the supplementary tables.

Acknowledgements

We sincerely appreciate thorough reviews from Editor Boswell Wing and two anonymous reviewers. We thank Junjie Jin from the Department of Natural Resources of Zhejiang Province and Xuejin Wu from NIGPAS, for their help in sampling, and Zihu Zhang and Yong Du from CUG for their help with geochemical analyses. This research is financially supported by National Natural Science Foundation of China (NSFC Grant No. 42030510 and 41802023), Chinese Academy of Sciences (Grant No. XDB26000000), Natural Science Foundation of Jiangsu Province (Grant No. BK20171103), the National Science and Technology Major Project (Grant No. 2017ZX05036-001-004) and China Scholarship Council (Grant No. 201804910207). Funding was provided to T.W.L. through the NASA Astrobiology Institute under Cooperative Agreement No. NNA15BB03A issued through the Science Mission Directorate and the NASA Interdisciplinary Consortia for Astrobiology Research.

This paper is a contribution to the IGCP 653 and 735.

Appendix A. Supplementary material

Supplementary material related to this article can be found online at <https://doi.org/10.1016/j.epsl.2022.117858>.

References

- Ader, M., Sansjøfrø, P., Halverson, G.P., Busigny, V., Trindade, R.I., Kunzmann, M., Nogueira, A.C., 2014. Ocean redox structure across the Late Neoproterozoic Oxygenation Event: a nitrogen isotope perspective. *Earth Planet. Sci. Lett.* 396, 1–13. <https://doi.org/10.1016/j.epsl.2014.03.042>.
- Albanesi, G.L., Barnes, C.R., Trotter, J.A., Williams, I.S., Bergström, S.M., 2020. Comparative Lower-Middle Ordovician conodont oxygen isotope palaeothermometry of the Argentine Precordillera and Laurentian margins. *Palaeogeogr. Palaeoclimatol. Palaeoecol.* 549, 109115. <https://doi.org/10.1016/j.palaeo.2019.03.016>.
- Algeo, T.J., Rowe, H., 2012. Paleoceanographic applications of trace-metal concentration data. *Chem. Geol.* 324, 6–18. <https://doi.org/10.1016/j.chemgeo.2011.09.002>.
- Algeo, T.J., Tribouillard, N., 2009. Environmental analysis of paleoceanographic systems based on molybdenum-uranium covariation. *Chem. Geol.* 268 (3–4), 211–225. <https://doi.org/10.1016/j.chemgeo.2009.09.001>.
- Algeo, T.J., Meyers, P.A., Robinson, R.S., Rowe, H., Jiang, G.Q., 2014. Icehouse-greenhouse variations in marine denitrification. *Biogeosciences* 11, 1273–1295. <https://doi.org/10.5194/bg-11-1273-2014>.
- Canfield, D.E., Raiswell, R., Westrich, J.T., Reaves, C.M., Berner, R.A., 1986. The use of chromium reduction in the analysis of reduced inorganic sulfur in sediments and shales. *Chem. Geol.* 54 (1–2), 149–155. [https://doi.org/10.1016/0009-2541\(86\)90078-1](https://doi.org/10.1016/0009-2541(86)90078-1).
- Chen, K., Hu, D., Zhang, X., Zhu, H., Sun, L., Li, M., Shen, Y., 2020. Minor $\Delta^{33}\text{S}$ anomalies coincide with biotic turnover events during the Great Ordovician Biodiversification Event (GOBE) in South China. *Glob. Planet. Change* 184, 103069. <https://doi.org/10.1016/j.gloplacha.2019.103069>.
- Cheng, M., Li, C., Zhou, L., Algeo, T.J., Zhang, F., Romaniello, S., Jin, C.S., Lei, L.D., Feng, L.J., Jiang, S.Y., 2016. Marine Mo biogeochemistry in the context of dynamically euxinic mid-depth waters: a case study of the lower Cambrian Niutitang shales, South China. *Geochim. Cosmochim. Acta* 183, 79–93. <https://doi.org/10.1016/j.gca.2016.03.035>.
- Dahl, T.W., Hammarlund, E.U., Anbar, A.D., Bond, D.P., Gill, B.C., Gordon, G.W., Knoll, A.H., Nielsen, A.T., Schovsbo, N.H., Canfield, D.E., 2010. Devonian rise in atmospheric oxygen correlated to the radiations of terrestrial plants and large predatory fish. *Proc. Natl. Acad. Sci. USA* 107, 17911–17915. <https://doi.org/10.1073/pnas.1011287107>.
- Deng, Y., Fan, J., Zhang, S., Fang, X., Chen, Z., Shi, Y., Wang, H., Wang, X., Yang, J., Hou, X., Wang, Y., Zhang, Y., Chen, Q., Yang, A., Fan, R., Dong, S., Xu, H., Shen, S., 2021. Timing and patterns of the Great Ordovician Biodiversification Event and Late Ordovician mass extinction: perspectives from South China. *Earth-Sci. Rev.* 220, 103743. <https://doi.org/10.1016/j.earscirev.2021.103743>.
- Edwards, C.T., Saltzman, M.R., Royer, D.L., Fike, D.A., 2017. Oxygenation as a driver of the Great Ordovician Biodiversification Event. *Nat. Geosci.* 10, 925–929. <https://doi.org/10.1038/s41561-017-0006-3>.
- Edwards, C.T., Jones, C.M., Quinton, P.C., Fike, D.A., 2022. Oxygen isotope ($\delta^{18}\text{O}$) trends measured from Ordovician conodont apatite using secondary ion mass spectrometry (SIMS): Implications for paleo-thermometry studies. *GSA Bull.* 134 (1–2), 261–274. <https://doi.org/10.1130/B35891.1>.
- Fan, J.X., Shen, S.Z., Erwin, D.H., Sadler, P.M., MacLeod, N., Cheng, Q.M., Hou, X.D., Yang, J., Wang, X.D., Wang, Y., Zhang, H., 2020. A high-resolution summary of Cambrian to Early Triassic marine invertebrate biodiversity. *Science* 367, 272–277. <https://doi.org/10.1126/science.aax4953>.
- Fang, X., Li, W., Zhang, J., Song, Y., Zhang, Y., 2020. Paleo-environmental changes during the Middle-Late Ordovician transition on the Yangtze Platform, South China and their ecological implications. *Palaeogeogr. Palaeoclimatol. Palaeoecol.* 560, 109991. <https://doi.org/10.1016/j.palaeo.2020.109991>.
- Gill, B.C., Dahl, T.W., Hammarlund, E.U., LeRoy, M.A., Gordon, G.W., Canfield, D.E., Anbar, A.D., Lyons, T.W., 2021. Redox dynamics of later Cambrian oceans. *Palaeogeogr. Palaeoclimatol. Palaeoecol.* 581, 110623.
- Goldberg, T., Archer, C., Vance, D., Thamdrup, B., McAnena, A., Poulton, S.W., 2012. Controls on Mo isotope fractionations in a Mn-rich anoxic marine sediment, Gullmar Fjord, Sweden. *Chem. Geol.* 296, 73–82. <https://doi.org/10.1016/j.chemgeo.2011.12.020>.
- Haq, B.U., Schutter, S.R., 2008. A chronology of Paleozoic sea-level changes. *Science* 322 (5898), 64–68. <https://doi.org/10.1126/science.1161648>.
- Higgins, M.B., Robinson, R.S., Husson, J.M., Carter, S.J., Pearson, A., 2012. Dominant eukaryotic export production during ocean anoxic events reflects the importance of recycled NH_4^+ . *Proc. Natl. Acad. Sci. USA* 109, 2269–2274. <https://doi.org/10.1073/pnas.1104313109>.
- Jin, J., Zhan, R., Wu, R., 2018. Equatorial cold-water tongue in the Late Ordovician. *Geology* 46, 759–762. <https://doi.org/10.1130/G45302.1>.
- Junium, C.K., Arthur, M.A., 2007. Nitrogen cycling during the Cretaceous, Conomanian-Turonian Oceanic Anoxic Event II. *Geochem. Geophys. Geosyst.* 8 (3). <https://doi.org/10.1029/2006GC001328>.
- Kah, L.C., Thompson, C.K., Henderson, M.A., Zhan, R., 2016. Behavior of marine sulfur in the Ordovician. *Palaeogeogr. Palaeoclimatol. Palaeoecol.* 458, 133–153. <https://doi.org/10.1016/j.palaeo.2015.12.028>.
- Kendall, B., Dahl, T.W., Anbar, A.D., 2017. The stable isotope geochemistry of molybdenum. *Rev. Mineral. Geochem.* 82, 683–732. <https://doi.org/10.2138/rmg.2017.82.16>.
- Kozik, N.P., Young, S.A., Bowman, C.N., Saltzman, M.R., Them, T.R., 2019. Middle-Upper Ordovician (Darriwilian-Sandbian) paired carbon and sulfur isotope stratigraphy from the Appalachian Basin, USA: implications for dynamic redox conditions spanning the peak of the Great Ordovician Biodiversification Event. *Palaeogeogr. Palaeoclimatol. Palaeoecol.* 520, 188–202. <https://doi.org/10.1016/j.palaeo.2019.01.032>.
- Lang, X., Tang, W., Ma, H., Shen, B., 2020. Local environmental variation obscures the interpretation of pyrite sulfur isotope records. *Earth Planet. Sci. Lett.* 533, 116056. <https://doi.org/10.1016/j.epsl.2019.116056>.
- Lenton, T.M., Dahl, T.W., Daines, S.J., Mills, B.J., Ozaki, K., Saltzman, M.R., Porada, P., 2016. Earliest land plants created modern levels of atmospheric oxygen. *Proc. Natl. Acad. Sci. USA* 113, 9704–9709. <https://doi.org/10.1073/pnas.1604787113>.
- Loureiro, M.J., Trull, T.W., Sigman, D.M., 2003. Sensitivity of $\delta^{15}\text{N}$ of nitrate, surface suspended and deep sinking particulate nitrogen to seasonal nitrate depletion in the Southern Ocean. *Glob. Biogeochem. Cycles* 17 (3). <https://doi.org/10.1029/2002GB001973>.
- Lu, W., Ridgwell, A., Thomas, E., Hardisty, D.S., Luo, G., Algeo, T.J., Saltzman, M.R., Gill, B.C., Shen, Y., Ling, H.F., Edwards, C.T., 2018. Late inception of a resiliently oxygenated upper ocean. *Science* 361, 174–177. <https://doi.org/10.1126/science.aar5372>.
- Marlow, J.R., Lange, C.B., Wefer, G., Rosell-Melé, A., 2000. Upwelling intensification as part of the Pliocene-Pleistocene climate transition. *Science* 290 (5500), 2288–2291. <https://doi.org/10.1126/science.290.5500.2288>.
- Nägler, T.F., Siebert, C., Lüschen, H., Böttcher, M.E., 2005. Sedimentary Mo isotope record across the Holocene fresh-brackish water transition of the Black Sea. *Chem. Geol.* 219, 283–295. <https://doi.org/10.1016/j.chemgeo.2005.03.006>.
- Nägler, T.F., Anbar, A.D., Archer, C., Goldberg, T., Gordon, G.W., Greber, N.D., Siebert, C., Sohrin, Y., Vance, D., 2014. Proposal for an international molybdenum isotope measurement standard and data representation. *Geostand. Geoanal. Res.* 38 (2), 149–151.
- Noordmann, J., Weyer, S., Montoya-Pino, C., Dellwig, O., Neubert, N., Eckert, S., Paetzzel, M., Böttcher, M.E., 2015. Uranium and molybdenum isotope systematics in modern euxinic basins: case studies from the central Baltic Sea and the Kyllaren fjord (Norway). *Chem. Geol.* 396, 182–195. <https://doi.org/10.1016/j.chemgeo.2014.12.012>.
- Poulton, S.W., Canfield, D.E., 2005. Development of a sequential extraction procedure for iron: implications for iron partitioning in continental derived particulates. *Chem. Geol.* 214, 209–221. <https://doi.org/10.1016/j.chemgeo.2004.09.003>.

- Poulton, S.W., Fralick, P.W., Canfield, D.E., 2004. The transition to a sulphidic ocean ~1.84 billion years ago. *Nature* 431, 173–177. <https://doi.org/10.1038/nature02912>.
- Prokopenko, M.G., Hammond, D.E., Berelson, W.M., Bernhard, J.M., Stott, L., Douglas, R., 2006. Nitrogen cycling in the sediments of Santa Barbara Basin and Eastern Subtropical North Pacific: Nitrogen isotopes, diagenesis and possible chemosymbiosis between two lithotrophs (*Thioploca* and *Anammox*)—“riding on a glider”. *Earth Planet. Sci. Lett.* 242, 186–204. <https://doi.org/10.1016/j.epsl.2005.11.044>.
- Saltzman, M.R., Edwards, C.T., 2017. Gradients in the carbon isotopic composition of Ordovician shallow water carbonates: a potential pitfall in estimates of ancient CO₂ and O₂. *Earth Planet. Sci. Lett.* 464, 46–54. <https://doi.org/10.1016/j.epsl.2017.02.011>.
- Saupe, E.E., Qiao, H., Donnadieu, Y., Farnsworth, A., Kennedy-Asser, A.T., Ladant, J.B., Lunt, D.J., Pohl, A., Valdes, P., Finnegan, S., 2020. Extinction intensity during Ordovician and Cenozoic glaciations explained by cooling and palaeogeography. *Nat. Geosci.* 13 (1), 65–70.
- Schoepfer, S.D., Shen, J., Wei, H., Tyson, R.V., Ingall, E., Algeo, T.J., 2015. Total organic carbon, organic phosphorus, and biogenic barium fluxes as proxies for paleocean productivity. *Earth-Sci. Rev.* 149, 23–52. <https://doi.org/10.1016/j.earscirev.2014.08.017>.
- Scotese, C.R., 2014. Atlas of Silurian and Middle-Late Ordovician Paleogeographic Maps (Mollweide Projection), Maps 73–80, Volumes 5, The Early Paleozoic, PALEOMAP Atlas for ArcGIS, PALEOMAP Project.
- Scott, C., Lyons, T.W., 2012. Contrasting molybdenum cycling and isotopic properties in euxinic versus non-euxinic sediments and sedimentary rocks: refining the paleoproxies. *Chem. Geol.* 324, 19–27. <https://doi.org/10.1016/j.chemgeo.2012.05.012>.
- Servais, T., Harper, D.A., 2018. The great Ordovician biodiversification event (GOBE): definition, concept and duration. *Lethaia* 51 (2), 151–164. <https://doi.org/10.1111/let.12259>.
- Servais, T., Owen, A.W., Harper, D.A., Kröger, B., Munnecke, A., 2010. The great Ordovician biodiversification event (GOBE): the palaeoecological dimension. *Palaeogeogr. Palaeoclimatol. Palaeoecol.* 294, 99–119. <https://doi.org/10.1016/j.palaeo.2010.05.031>.
- Song, Y.Y., Yu, S.Y., Zhang, Y.D., Sun, X.W., Muir, L.A., Liu, P.J., 2017. Reconstruction of a shallow intraplatform depression by microfacies analysis of the Upper Ordovician Miaopo and Datianba formations in the northwestern Yangtze Region, China. *Palaeoworld* 26, 589–601. <https://doi.org/10.1016/j.palwor.2017.03.003>.
- Sperling, E.A., Melchin, M.J., Fraser, T., Stockey, R.G., Farrell, U.C., Bhajan, L., Bruno, T.N., Cole, D.B., Gill, B.C., Lenz, A., Loydell, D.K., 2021. A long-term record of early to mid-Paleozoic marine redox change. *Sci. Adv.* 7, eabf4382. <https://doi.org/10.1126/sciadv.abf4382>.
- Stockey, R.G., Cole, D.B., Planavsky, N.J., Loydell, D.K., Frýda, J., Sperling, E.A., 2020. Persistent global marine euxinia in the early Silurian. *Nat. Commun.* 11, 1–10. <https://doi.org/10.1038/s41467-020-15400-y>.
- Taylor, S.R., McLennan, S.M., 1985. *The Continental Crust: Its Composition and Evolution*. Blackwell, Oxford. 312 pp.
- Trotter, J.A., Williams, I.S., Barnes, C.R., Lécuyer, C., Nicoll, R.S., 2008. Did cooling oceans trigger Ordovician biodiversification? Evidence from conodont thermometry. *Science* 321, 550–554. <https://doi.org/10.1126/science.1155814>.
- Wallace, M.W., Shuster, A., Greig, A., Planavsky, N.J., Reed, C.P., 2017. Oxygenation history of the Neoproterozoic to early Phanerozoic and the rise of land plants. *Earth Planet. Sci. Lett.* 466, 12–19. <https://doi.org/10.1016/j.epsl.2017.02.046>.
- Young, S.A., Saltzman, M.R., Foland, K.A., Linder, J.S., Kump, L.R., 2009. A major drop in seawater ⁸⁷Sr/⁸⁶Sr during the Middle Ordovician (Darriwilian): links to volcanism and climate? *Geology* 37, 951–954. <https://doi.org/10.1130/G30152A.1>.
- Young, S.A., Gill, B.C., Edwards, C.T., Saltzman, M.R., Leslie, S.A., 2016. Middle-Late Ordovician (Darriwilian-Sandbian) decoupling of global sulfur and carbon cycles: isotopic evidence from eastern and southern Laurentia. *Palaeogeogr. Palaeoclimatol. Palaeoecol.* 458, 118–132. <https://doi.org/10.1016/j.palaeo.2015.09.040>.
- Zhang, J., Edwards, C.T., Diamond, C.W., Lyons, T.W., Zhang, Y., 2021. Marine oxygenation, deoxygenation, and life during the Early Paleozoic: an overview. *Palaeogeogr. Palaeoclimatol. Palaeoecol.* 584, 110715. <https://doi.org/10.1016/j.palaeo.2021.110715>.